



Catalytic behavior of Ru supported on Ce_{0.8}Zr_{0.2}O₂ for hydrogen production

I.A. Carbajal-Ramos^{a,b,*}, M.F. Gomez^c, A.M. Condó^{a,b}, S. Bengió^{a,b}, J.J. Andrade-Gamboa^a, M.C. Abello^c, F.C. Gennari^{a,b}

^a Centro Atómico Bariloche (CNEA) and Instituto Balseiro (UNCuyo), Av. Bustillo km 9.5, 8400 S.C. de Bariloche, Río Negro, Argentina

^b Consejo Nacional de Investigaciones Científicas y Técnicas (CONICET), Av. Bustillo km 9.5, 8400 S.C. de Bariloche, Río Negro, Argentina

^c Instituto de Investigaciones en Tecnología Química—(UNSL-CONICET), Chacabuco y Pedernera, 5700 San Luis, Argentina

ARTICLE INFO

Article history:

Received 19 April 2015

Received in revised form 30 June 2015

Accepted 16 July 2015

Available online 28 July 2015

Keywords:

Ruthenium

Ceria

Ethanol steam reforming

Hydrogen production

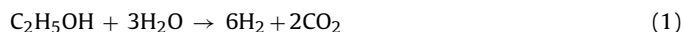
ABSTRACT

Ru (2 wt.%) on Ce_{0.8}Zr_{0.2}O₂ catalysts were investigated to test their ethanol steam reforming (ESR) performance. The supports were obtained through two different synthesis methods: co-precipitation (PI) and mechanochemical reaction (MR). Characterization of the catalysts, before and after ESR, were performed using X-ray powder diffraction (XRPD), nitrogen physisorption, CO chemisorption, temperature programmed reduction (TPR), high resolution transmission electron microscopy (HR-TEM), thermogravimetry, and X-ray photoelectron spectroscopy (XPS) measurements. The Ru (2 wt.%) PI catalyst exhibited the highest activity and selectivity to hydrogen and no coke deposition was observed during catalytic operation, even when compared to Ni (8 wt.%) PI catalyst. A possible reaction pathway is proposed. The remarkably good catalytic performance of Ru (2 wt.%) PI is regarded as being due to a combination of factors: improved metal dispersion on Ce_{0.8}Zr_{0.2}O₂, favorable metal-support interaction and water gas shift reaction promotion.

© 2015 Elsevier B.V. All rights reserved.

1. Introduction

The current energy panorama (high energy consumption, limited fuel fossil reserves, and environmental constraints, among others) demands the development of alternative energy sources, clean and renewable, which contribute to sustainable social development. Hydrogen emerges as a promising option, due to its high energetic density and clean combustion. Furthermore, it could be obtained from renewable sources. However, in order to produce hydrogen in a clean, safe and efficient way, some scientific and technological challenges still need to be overcome. Nowadays, the exploitation of natural sources like biomass instead of oil as feedstock is increasingly drawing more attention. Therefore, the production of hydrogen by Ethanol Steam Reforming (ESR) is an efficient way to satisfy the hydrogen demand from a renewable and environment-friendly energy source. The overall ESR reaction can be expressed stoichiometrically as:



The reforming process may be considered to be the combination of the ESR to syngas ($\text{H}_2 + \text{CO}$, Eq. (2)) followed by water gas shift reaction (WGS, Eq. (3)).



The aims of the Eq. (1) are a high yield to H_2 and a high selectivity toward CO_2 . Nevertheless, there are several side reactions which could lead to the production of compounds such as CH_4 , $\text{C}_2\text{H}_4\text{O}$, C_2H_4 , $\text{C}_3\text{H}_6\text{O}$ (among others), and therefore, affect the expected hydrogen yield. Literature reports reveal that ethanol conversion and selectivity to hydrogen strongly depend on the nature of the metal and the support, the type of precursor, the preparation methods, the presence of additives and the operating conditions [1].

In order to elucidate which catalytic system is more suitable [1–35], different systems have been investigated for ESR, on a variety of supports, with noble (Pd, Pt, and Rh) and non-noble metals (Co, Ni, Cu). Among these, Rh, Ni, and Co show the best performance and constitute the most studied catalytic systems [2–5,7–29,32,34,35]. Auaprête et al. [29] studied different active phases (Rh, Pt, Pd, Ru, Ni, Cu, Zn, Fe) as well as supports (Al_2O_3 , CeO_2 – Al_2O_3 , CeO_2 , CeO_2 – ZrO_2 , ZrO_2) in order to obtain highly active catalysts for the ESR. It was found that Rh- and Ni-based

* Corresponding author at: Centro Atómico Bariloche (CNEA), R8402AGP, S.C. de Bariloche, Argentina. Fax: +54 294 4445190.

E-mail address: persisrai21@gmail.com (I.A. Carbajal-Ramos).

systems were the most active and selective, which achieved the highest H_2 yield over the Rh/CeZrO₂ catalyst. Liguras et al. [9] studied ESR over Rh, Ru, Pt, and Pd supported on Al₂O₃, MgO, TiO₂. Rh catalysts have shown higher ethanol conversion and hydrogen production than Ru, Pt, and Pd. However, only at relatively high Ru loading (5 wt.%) hydrogen production on Ru-based catalysts was comparable to Rh. The inconvenience with Ru catalysts was the high coke production, which results from the dehydration of ethanol to ethylene promoted by Ru. Although Bilal and Jackson [36] found that Ru/Al₂O₃ had a high selectivity to hydrogen, it produced high levels of ethylene, methane and carbon monoxide, and high quantities of carbonaceous deposit. In order to solve this problem, suitable promoters/additives which prevent coke formation are required.

The nature of the support may strongly influence the catalytic performance of ESR catalysts and even take part in the reaction. To avoid carbon deposit formation, a basic support, such as CeO₂ could be used as an alternative solution. This material possesses exceptional qualities, such as high oxygen mobility, high oxygen storage capacity (OSC), strong interaction with the supported metal and the excellent capacity to promote high dispersion of noble metals [37,38]. These qualities render this material as promising for catalysis. In particular, when ZrO₂ to CeO₂ lattice is added, the ceria redox properties are enhanced: CeO₂ basicity is reduced as the ZrO₂ content is increased, CeO₂ thermal resistance is improved and metal dispersion is increased. Ceria based materials are largely present in Three-Way Catalysts [39,40], and are active for the selective oxidation of carbon monoxide and for the promotion of the WGS [41–45]. During oxidation of carbon monoxide, mobile oxygen present in ceria can react with CO, as oxygen re-oxidizes the reduced ceria. As CeO₂ can enhance the rate of one of the main steps (water dissociation) [27,42–45] due to the existence of O vacancies and Ce³⁺, it is considered to be the key in WGS pathways.

The noble metals deposited on ceria could interact with the support and promote its reduction. They are also used for ethanol and glycerol steam reforming [46,47] as well as for Solid Oxide Fuel Cells (SOFCs) electrodes [48]. In fact, in our previous research, Ru/CeO₂/YSZ showed good activity and stability for ESR, with low coke production. Hence, this metal-support combination seems to be a promising catalyst for ESR [49]. Recently, Yaseneva et al. [50] modified the Ce_xZr_{1-x}O₂ support by introducing La, Pr, and Sm into Ru and Pt supported catalysts: Ce_xZr_{1-x}(La, Pr, Sm)_{1-2x}O₂/Al₂O₃. Results showed that Ru-containing catalysts doped by Sm were the most effective whereas La-doping led to the most active catalyst among the Pt-based ones.

In the present work, the activity and stability of Ru supported on Ce_{0.8}Zr_{0.2}O₂ catalysts for ESR were evaluated. In order to compare their performance, Ni on Ce_{0.8}Zr_{0.2}O₂ was also synthesized and tested for ESR under the same experimental conditions. The synergistic effect between Ru metal nanoparticles and CeO₂ based support for ESR was analyzed.

2. Experimental

2.1. Catalyst preparation

Ceria–zirconia mixed oxides with nominal composition 0.8Ce:0.2Zr:2O were synthesized using two different methods: co-precipitation technique (PI) and mechanochemical reaction (MR). In the former, a mixture of Ce(NO₃)₃·6H₂O (Aldrich 99.99%) and Zr(NO₃)₂·xH₂O (Aldrich, 99.99%) aqueous solutions was added dropwise to an ammonia solution. Cerium oxidation was completed by adding H₂O₂ (30% v/v) and the obtained solution was kept under vigorous stirring for 0.5 h. The product was filtered, suspended in isopropanol and stirred under reflux for 6 h [51].

Finally, the sample was dried overnight at 120 °C and then calcined in air at 600 °C for 5 h. The final sample is hereafter indicated as PI.

In the mechanochemical method, the starting materials used were anhydrous CeCl₃ (Aldrich, purity 99.99%), anhydrous ZrCl₄ (Merck, purity 99.9%) and NaOH (Biopack, purity 98%). All reactants were weighed in an argon-filled glove box, with moisture maintained below 1 ppm. The mixture of CeCl₃–ZrCl₄–NaOH with a 0.8:0.2:3.2 molar ratio was ball milled at 400 rpm in air at room temperature for 5 h. The milling was carried out in a planetary ball mill (Fritsch Pulverisette P6), using both vial and balls of stainless steel. A ball to powder weight ratio of 80:1 was employed. After milling, the samples were washed with distilled water in order to eliminate the NaCl produced as sub-product of the reaction. The samples were then submitted to calcination at 600 °C for 5 h [52]. The final sample is hereafter indicated as MR.

Ru (2 wt.%) was supported onto PI and MR by a wet impregnation method using an aqueous solution of Ru(NO)(NO₃)_x(OH)_y, $x + y = 3$ (Aldrich, 99.9%). Ni (8 wt.%) was supported only on PI by the same impregnation method, using an aqueous solution of Ni(NO₃)₂ (Aldrich, 99.99%). The appropriate amount of the metal precursor was dissolved in distilled water. Then, the support in powder was added and the suspension was stirred for 2 h. The solvent was removed at reduced pressure and the solid was dried at 120 °C overnight. Finally, the samples were calcined in a static oven at 600 °C for 5 h (heating rate 5 °C min⁻¹). These catalysts are designated as RuPI, RuMR and NiPI.

2.2. Catalyst characterization

Structural and microstructural changes were studied employing X-ray Powder Diffraction (XRPD, Philips PW 1710/01 Instruments), using CuK α radiation and graphite monochromator. X-ray diffractograms were collected using a step size of 0.02° and a counting time of 1 s. Cell parameters of the solid solution Ce_xZr_{1-x}O₂ were calculated with CELREF software [53]. The Lorentzian and the Gaussian component to peak breadth were calculated from the single peak profile analysis, performed on (1 1 1) reflection of the Ce_{0.8}Zr_{0.2}O₂. The Lorentzian component (β_L) allowed to calculate the mean crystallite size from Scherrer equation ($\beta_L = \frac{K\lambda}{D_{hkl}\cos\theta}$) and the Gaussian component (β_G) allowed to calculate microstrain as $\epsilon = \frac{\beta_G}{4\tan\theta}$ [54]. For instrumental breadth calculation, a sample of CeO₂ annealed to 1000 °C during 24 h and then slowly cooled down, was used as a pattern.

Textural characteristics of the samples were studied using a Micromeritics ASAP 2020 analyzer. N₂ adsorption isotherms were collected at –196 °C on 0.2 g of sample, after evacuation at 350 °C overnight. Surface area and pore distribution were obtained applying the BET and BJH methods, respectively.

Temperature Programmed Reduction (TPR) and CO chemisorption experiments were performed using Thermal Conductivity Detector (TCD) in a Micromeritics AutoChem 2910 instrument. For the TPR measurements, average samples of 0.25 g were cleaned for 1 h at 350 °C by pulsing O₂ in an Ar flow every 75 s. Then, they were purged with Ar at 350 °C for 15 min and cooled to –70 °C. The H₂ (5%)/Ar (40 mL min⁻¹) mixture was admitted into the reactor and the flow was stabilized for 30 min before increasing the temperature to 900 °C at 5 °C min⁻¹.

CO chemisorption experiments at 40 °C were used to determine dispersion and average size of metallic particles supported on Ce_{0.8}Zr_{0.2}O₂ [49,55]. The following procedure was applied in the measurements: firstly, the catalysts (typically 0.2 g) were subjected to a cleaning pretreatment at 300 °C for 1 h under O₂ (30%)/Ar flow. Then, they were reduced to ensure the metallic state of Ru or Ni particles supported onto Ce_{0.8}Zr_{0.2}O₂. For this purpose an H₂ (5%)/Ar flow was used for 1 h at a chosen temperature based

on the TPR results. For Ru and Ni catalysts, the selected reduction temperature was 200 °C and 600 °C, respectively. Then, the chemisorption was carried out with He carrier (50 mL min⁻¹) and reactive gas CO (pulses of 0.4853 mL). A purge with He flow at 40 °C was then performed. In order to avoid the so-called reversible adsorption, chemisorption was repeated. A CO:metal chemisorption stoichiometry = 1:1 and a spherical geometry were assumed to calculate the particle diameter.

High-resolution transmission electron microscopy (HR-TEM) studies were performed using a TEM Philips CM200 UT operating at 200 kV. Samples for TEM were prepared by dispersing a small amount of powder in hexane and depositing a drop of the resulting suspension on a commercial holey-carbon coated copper grid. The mean crystallite size of the supports was determined statistically (as arithmetic mean), measuring 60 crystallites of the dark field micrographs.

Surface composition was analyzed by means of X-ray photoelectron spectroscopy (XPS) using a standard Al/Mg twin-anode X-ray gun and a hemispherical electrostatic electron energy analyzer. The measurements were carried out in high vacuum conditions (HV), with a base pressure of ~10⁻⁹ Torr. For the analysis, the powdered samples were spread on an adhesive graphitic carbon tape. The overall energy scale was calibrated with the Zr3d main component and the O1s lattice component at binding energies 181.7 eV and at 528.8 eV, respectively.

Thermogravimetric analyses (TGA) were performed using a TA Instruments HP50 equipment. In most samples 10–20 mg of the spent catalysts were loaded in a quartz crucible. The temperature was increased up to 800 °C at a heating rate of 10 °C min⁻¹ in a mixture of O₂ (10%)/N₂ of 60 mL min⁻¹.

2.3. Catalytic tests

The ethanol steam reforming (ESR) activity measurements were carried out under three different sets of experimental conditions: moderate, severe and soft (Table 1). The ethanol/water ratio was invariable (with a value of 5). The catalytic tests were performed using two apparatuses, one for soft conditions, and the other for moderate and severe conditions.

The equipment used for moderate and severe conditions contains a tubular fixed-bed quartz reactor operated at atmospheric pressure. The reactor is encased in a furnace which is regulated by a programmable temperature controller. The reaction temperature was measured with a coaxial thermocouple. The feed was a gas mixture of ethanol, water and helium (free of oxygen). The C₂H₅OH/H₂O 1:5 mixture was fed through an isocratic pump. The catalyst weight of 50 mg (0.3–0.4 mm) was diluted with quartz of the same mesh (1:2 weight ratio). The particle size range (0.3–0.4 mm) was selected after preliminary mass transport experiments to minimize diffusional resistances. Before testing the catalytic activity, the materials were activated by reduction in H₂ flow during 30 min, at 150 °C for Ru samples and at 600 °C for NiPI. Then, the catalyst was purged and heated to the reaction temperature under a He flow. Afterwards, the C₂H₅OH + H₂O mixture was admitted into the reactor to carry out the catalytic test. The reactants and reaction products were analyzed on-line by gas chromatography. H₂, CH₄, CO₂, and H₂O were separated by a 1.8 m carboxosphere (80–100 mesh) column and analyzed by TCD. Nitrogen was used as an internal standard. Separately, CO was analyzed by a flame ionization detector (FID) after being passed through a methanizer. Higher hydrocarbons and oxygenated products (C₂H₄O, C₂H₄, C₃H₆O, C₂H₅OH, etc.) were separated in a RT-U PLOT capillary column and analyzed with FID using N₂ as carrier gas. The homogeneous contribution was tested in the empty reactor. These runs showed no activity at 500 °C whereas the ethanol conversion was 3% at 600 °C, and acetaldehyde was the only formed product.

The second apparatus was only used for experimental runs under soft conditions. It includes a U-shaped 4 mm internal diameter quartz microreactor. Typically 30 mg of catalyst were used, diluted in a 1:2 weight ratio with high purity α-Al₂O₃ (Grace Davison, calcined at 1300 °C for 24 h). C₂H₅OH/H₂O 1:5 mixture was injected into an Ar flow with a Hamilton Gastight syringe using an INSTECH Model 2000 syringe pump at a rate of 1.8 μL min⁻¹. All transfer lines between syringe, reactor and GC were heated to 120 °C. Before testing the catalytic activity, the materials were pretreated under O₂(5%)/Ar at 350 °C for 1 h (40 mL min⁻¹, 10 °C min⁻¹) and activated by reduction in H₂(5%)/Ar for 2 h (40 mL min⁻¹, 5 °C min⁻¹) at 150 °C for Ru samples and at 600 °C for NiPI. The gaseous mixture was first introduced in the reactor at 150 °C for 1 h. The furnace temperature was then increased to 600 °C with a heating rate of 1 °C min⁻¹. After 2 h at 600 °C, the furnace was cooled to 150 °C at the same rate. The catalyst underwent two of these cycles before being tested isothermally at selected temperatures. On-line GC analysis was performed using a Hewlett Packard 5890 Series II gas chromatograph. A Molsieve 5A column with Ar as carrier was connected to a TCD to analyze H₂, O₂, N₂, CH₄, and CO. A PoraPLOT Q column, with He as carrier, was connected in series to a methanizer and to a FID to analyze the carbon-containing compounds. Carbon balance was always within ±2%.

Ethanol conversion (X_{EtOH}) selectivity to products (S_i) and selectivity to hydrogen (S_{H_2}) are defined as follows:

$$X_{\text{EtOH}} = \frac{F_{\text{EtOH}}^{\text{in}} - F_{\text{EtOH}}^{\text{out}}}{F_{\text{EtOH}}^{\text{in}}} \times 100 \quad (4)$$

$$S_i = \frac{\nu_i F_i^{\text{out}}}{2 (F_{\text{EtOH}}^{\text{in}} - F_{\text{EtOH}}^{\text{out}})} \times 100 \quad (5)$$

$$S_{\text{H}_2} = \frac{F_{\text{H}_2}^{\text{out}}}{6 (F_{\text{EtOH}}^{\text{in}} - F_{\text{EtOH}}^{\text{out}})} \times 100 \quad (6)$$

being F_i^{in} and F_i^{out} the molar flow rates of product “i” at the inlet and outlet of the reactor, respectively and ν_i the number of carbon atoms in “i”.

3. Results and discussion

3.1. Characterization of Ru-catalysts

Table 2 summarizes the structural, microstructural, and textural characterization of the bare supports (PI and MR) and the catalysts (RuPI and RuMR). The supports were characterized by XRPD measurements. The diffraction patterns confirm the presence of the fluorite type lattice (see Fig. S1-a in Supplementary material). Within the detection limits of the XRPD technique, there is no evidence of the presence of tetragonal (t-) or monoclinic (m-) ZrO₂ phases or segregation of solid solution with a composition other than Ce_{0.8}Zr_{0.2}O₂. By comparison with the standard CeO₂ (PDF 34-0394), the peaks corresponding to PI and MR shifted to greater 2θ values. This result indicates Zr incorporation according to Vegard's law, where a linear decrease of the lattice parameter with x in Ce_{1-x}Zr_xO₂ is expected because the Zr⁴⁺ radius (0.084 nm) is less than that of Ce⁴⁺ (0.097 nm). The x value was calculated by using the relation $a_x = a_0 - 0.027x$ [56], where a_0 and a_x are the cell parameters (in nm) for pure CeO₂ and solid solutions, respectively (Table 2). For Ru samples the most intense peaks of RuO₂ phase were overlapped with the Ce_{0.8}Zr_{0.2}O₂ support. Therefore, the XRPD patterns were collected on both samples after activation (H₂ reduction at 200 °C). No differences were observed with the bare support pattern (see Fig. S1-b and S1-c in Supplementary material). This is probably due to the low amount of Ru (2 wt.%) and/or the smaller Ru

Table 1

Experimental conditions for ethanol steam reforming reaction.

Parameters	Slight conditions	Moderate conditions	Severe conditions
$F_{\text{EtOH}}^{\text{in}}$ (mol min ⁻¹) ^a	1.22×10^{-5}	1.02×10^{-3}	1.02×10^{-3}
Inlet ethanol concentration, (%) ^b	1	7.5	9.5
W (mg) ^c	30	50	50
$\frac{W}{F_{\text{EtOH}}^{\text{in}}}$ (g min mol ⁻¹)	2447	49	49
Catalysts dilution ^d	33%	33%	33%
GHSV (mL g ⁻¹ h ⁻¹) ^e	60 000	370 000	290 000
Carrier	Ar	He	He
Reaction temperature (°C)	200–600, 1 °C/min	600	500–550–600

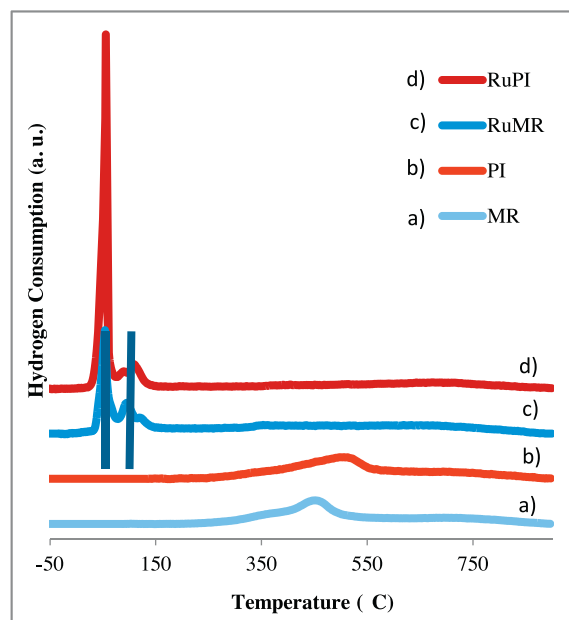
^a Initial ethanol molar flow [mol min⁻¹].^b Inlet ethanol concentration = $F_{\text{EtOH}}^{\text{in}}/F_T^{\text{in}}$ [%].^c W = Catalyst weight [g].^d Catalyst dilution = $W/(W + D)$ [%], D = diluent weight [g].^e GHSV (gas hourly space velocity) = $F_T^{\text{in}} V_{m60}/W$ [mL g⁻¹ h⁻¹], F_T^{in} = total initial molar flow [mol min⁻¹], V_m = molar volume [mL mol⁻¹] = 22,400 mL mol⁻¹ under STP.**Table 2**Structural, microstructural and textural characterization of Ru catalysts and bare Ce_{0.8}Zr_{0.2}O₂ supports.

Sample		PI	RuPI	MR	RuMR
Technique					
N ₂	SSA ^a (m ² g ⁻¹)	118	108	48	36
physisorp-	CPV ^b (mL g ⁻¹)	0.37	0.36	0.16	0.14
tion	dM ^c (nm)	10	13	16	11
XRPD	Support mean crystallite size ^d (nm)	5	6	12	12
	α_x Cell parameter ^e (nm)	0.5376	–	0.5364	–
CO	Metallic dispersion ^f (%)	–	64.1	–	37.4
chemisorp-	Apparent particle size ^g (nm)	–	2.2	–	3.7
tion	Metallic specific surface area ^g (m ² /g sample)	–	5.6	–	3.2
	Metallic specific surface area ^g (m ² /g metal)	–	278.1	–	162.3

^a Specific surface area from BET analysis.^b Cumulative Pore Volume determined from the desorption branch of physisorption isotherms.^c Relative maxima of the pore distribution determined by the BJH analysis from the desorption branch of the physisorption isotherms.^d From Scherrer's formula.^e Calculated using CELREF software.^f Assuming a CO/M stoichiometry of 1.^g Calculated assuming a spherical geometry of the metal particles.

particles which are not detectable by this technique. N₂ physisorption at liquid nitrogen temperature was employed to investigate the textural properties of the samples. The PI and MR supports were highly porous with Type IV isotherms, and showed the presence of a mesoporous network [57] (Fig. S2a in Supplementary material). On the one hand, the PI isotherm showed a H3 type hysteresis loop which exhibited no limiting adsorption at high p/p° . This indicates the presence of agglomerates of particles forming slit shaped pores (plates or edged particles like cubes) with non-uniform size and/or shape [58,59]. The BET specific surface area calculated was 118 m²/g (Table 2). On the other, the MR isotherm showed an H2 type hysteresis loop which suggests the presence of pores with not well-defined size and shape [58]. The BET specific surface area was 48 m²g⁻¹, about half the area of PI. By applying the BJH method to the desorption branch of the isotherm (see Fig. S2b in Supplementary material), MR showed a narrow pore size distribution (from 10 nm to 20 nm), whereas the PI support presented a wider distribution (5–40 nm), centered at 10 nm. The impregnation with the precursor metal slightly decreases the surface area, from 118 m²/g to 108 m²/g for PI and 48 m²/g to 36 m²/g for MR, maintaining the same type of isotherms and the type of porosity.

Temperature Programmed Reduction experiments were performed to assess the reducibility of the materials and to select the best conditions for the catalyst activation before catalytic experiments (complete reduction of the metal phases). TPR tests were performed starting from –70 °C in order to obtain information about the reduction of ruthenium oxide at low temperature. The TPR profiles for MR and PI were very similar (Fig. 1a and b). For both samples, the reduction started at 250 °C, and led to a very broad peak between 350 °C and 550 °C. In addition, a weak shoulder

**Fig. 1.** TPR profiles for: (a) PI, (b) MR, (c) RuPI, and (d) RuMR.

was observed around 700 °C. Notably, surface and bulk reduction of Ce_xZr_{1-x}O₂ materials can occur at the same temperature [60], which could explain the similarity in the TPR profiles despite some differences in the textural properties (surface area, pore size distribution and crystalline size). Due to this phenomenon, the first

reduction zone (350–500 °C) was assigned to the reduction of surface and bulk reduction of $\text{Ce}_{0.8}\text{Zr}_{0.2}\text{O}_2$ [5]. Considering the bulk homogeneity of both samples, the second zone can be mainly associated to baseline drift due to sample sintering/compacting that can occur during the TPR and give rise to an apparent H_2 uptake [60].

A slight difference was observed in the first maximum zone, 500 °C for PI and 450 °C for MR. As a consequence of the preparation method, the MR support was slightly contaminated with Fe (<5 at.%) [52]. The decrease of the peak temperature could be associated with iron incorporation in $\text{Ce}_{0.8}\text{Zr}_{0.2}\text{O}_2$, in agreement with previous studies [61]. However, from XRPD measurements, neither Fe_2O_3 in MR was detected after thermal treatment up to 900 °C nor it was possible to confirm structural incorporation of Fe due to the negligible effect on cell parameters of the fluorite type lattice [62]. Lattice oxygen is more labile in $\text{Ce}_{1-x}\text{Fe}_x\text{O}_{2-\delta}$ [62] and there is more formation of surface oxygen and bulk oxygen suitable in $\text{Ce}_{1-x}\text{Fe}_x\text{O}_{2-\delta}$ than CeO_2 . As in a previous study, these factors could be translated into better reducibility properties of CeO_2 containing Fe [62].

TPR profiles of RuMR and RuPI are shown in Fig. 1c and d. Both profiles are very similar and they present two sharp reduction peaks centered at 55 °C and 100 °C, assigned to highly dispersed RuO_2 and larger RuO_2 crystallites, respectively [63–65]. The presence of an easily reducible metal oxide (such as ruthenium oxide) significantly promotes the reduction of cerium [66]. The amounts of hydrogen consumption at low temperature (see next paragraph) point out that the reduction temperature of Ce^{+4} to Ce^{+3} seems to be below 150 °C. Remarkably, the bare support showed a reduction onset temperature around 500 °C. This result evidences the strong metal support interaction between Ru and $\text{Ce}_{0.8}\text{Zr}_{0.2}\text{O}_2$. Then, the amount of hydrogen consumption at low temperature (less than 150 °C) corresponds to the reduction of both, the supported metal oxide and the support. Moreover, the disparity in the intensity of the peaks indicates different amount of hydrogen consumption for each support. As RuPI and PI samples present no impurities, the hydrogen consumption associated with the sample reduction was evaluated only for these cases [52].

The areas under TPR profiles were evaluated below 550 °C, considering that the main hydrogen consumption occurred at lower temperatures and that the surface area could be modified at temperatures over 600 °C. The bare support PI had a hydrogen consumption of 1121 $\mu\text{mol/g}$ whereas for RuPI, hydrogen consumption was 1589 $\mu\text{mol/g}$. Considering only the hydrogen consumption below 150 °C for RuPI, it was 1438 $\mu\text{mol/g}$. The small differences between both consumptions (below 550 °C and below 150 °C) could be an integration error, so we can conclude that the reduction of RuPI is below 150 °C. The theoretical hydrogen consumption to reduce all the ruthenium is 396 $\mu\text{mol/g}$ (considering ruthenium as RuO_2). Therefore, the metal was completely reduced whereas the support was reduced in the same extension as in the bare support. Even though the integration of the peaks may induce a non-negligible error, the estimation serves as indicators of the processes occurring as temperature increases.

CO chemisorption was employed to evaluate the accessibility of the metal phases (Table 2). Ru2PI presented a higher metal accessibility than RuMR (64.1% and 37.4%, respectively) and, hence, a higher metallic dispersion value is inferred. This result is directly correlated with the surface area of each support obtained from physisorption studies. The RuMR metallic specific area was about two times smaller than RuPI, which evidences the influence of the support preparation method (MR area is approximately half the PI area). The apparent Ru particle size is lower than 4 nm. Despite of this value cannot be compared directly with that measured by HR-TEM combined with EDS analysis (see further in Section 3.3), they are in the same order. High values of dispersion are in accor-

dance with the strong metal-support interaction that favors higher dispersions noble metals [66,67].

3.2. Catalytic activity in ESR for Ru catalysts

Fig. 2a and b show the result of ESR on RuPI and RuMR under soft conditions. The performances of both catalysts were very similar. RuPI (Fig. 2a) showed a progressive increase in the ethanol conversion up to 450 °C, while RuMR (Fig. 2b) displayed an increase up to 500 °C. Simultaneously, H_2 selectivity continuously increased reaching at 570 °C a maximum of S_{H_2} = 88.9% for PI and S_{H_2} = 89.7% for MR. Between 200 °C and 500 °C, along with the formation of hydrogen, carbon dioxide and acetone, low amounts of by-products, such as acetaldehyde and methane (selectivities always below 15%) were generated. CO production was significant only above 400 °C. After complete ethanol conversion (above 500 °C), only H_2 , CO, and CO_2 were detected in the gas phase, with an expected relative ratio for WGSR equilibrium at this temperature. The similar kinetic behavior between RuPI and RuMR under soft conditions can be attributed to an excess in active sites, showing no differences.

The study of the RuPI and RuMR catalytic activity as a function of temperature for ethanol steam reforming under soft conditions gives an accurate panorama of the catalyst reactivity. In order to specify the role of the support and to analyze the catalyst in real operating conditions, the Ru catalysts were tested at 600 °C (the highest temperature analyzed in Fig. 2), shifting to stronger conditions.

Figs. S3a and S3b show the results of ethanol steam reforming on the supports (PI and MR) under moderate conditions at 600 °C for 10 h. Ethanol conversion was complete for PI support during 500 min in time on stream (Fig. S3a) and the main product was ethylene ($S_{\text{C}_2\text{H}_4}$ = 70%). Minor amounts of H_2 , CO_2 , CH_4 , and $(\text{CH}_3)_2\text{CO}$ were also detected. Ethylene is produced by ethanol dehydration, which is a strong promoter of coke formation. On MR supports, ethanol conversion decreased from an initial value of 100% to 90% in 500 min (Fig. S3b). Although the main product obtained was ethylene (ethanol dehydration), an important amount of acetone was also detected. Only minor amounts of H_2 , CO_2 , and CH_4 were produced. Acetone production is promoted by CeO_2 -based materials (at temperatures below 360 °C) [68] and basic oxides, such as Fe_2O_3 [69]. Unlike ethylene, acetone was not formed under the selected experimental conditions (Fig. S3a). The differences observed between both supports could be ascribed to iron contamination introduced during synthesis of MR [52]. Basic oxides as Fe_2O_3 promote acetone formation [69,70] if the support is not reduced or the reduction is performed at low temperatures. Then, as the MR support was not reduced before the test, the reaction was consequently selective to acetone.

Fig. 3a shows the results of ethanol steam reforming on RuPI obtained at 600 °C under moderate conditions. The catalyst was very active with a complete ethanol conversion during 500 min in time on stream. Hydrogen selectivity was high (average of 93%), CO_2 selectivity was 60% and the only by-products were CO and CH_4 (acetone and acetaldehyde were not observed). CO/CO_2 ratio was 0.44, a very good ratio respect to the WGSR at this temperature (0.65 [71]), produced by the action of the support. The methane selectivity was relatively high (15%). The RuMR performance under the same conditions was quite similar (Fig. 3b), with an average X_{EtOH} = 92%, S_{H_2} = 68% and a CO/CO_2 ratio of 0.46. The methane selectivity was relatively high (S_{CH_4} = 14%). The carbon balance in both samples was almost 100%.

In order to study the catalyst performance in less favorable conditions, Ru catalysts were evaluated under severe conditions (see Section 2). RuPI (Fig. 4a) again presented an excellent activity, with a constant ethanol conversion of 100% during 600 min in

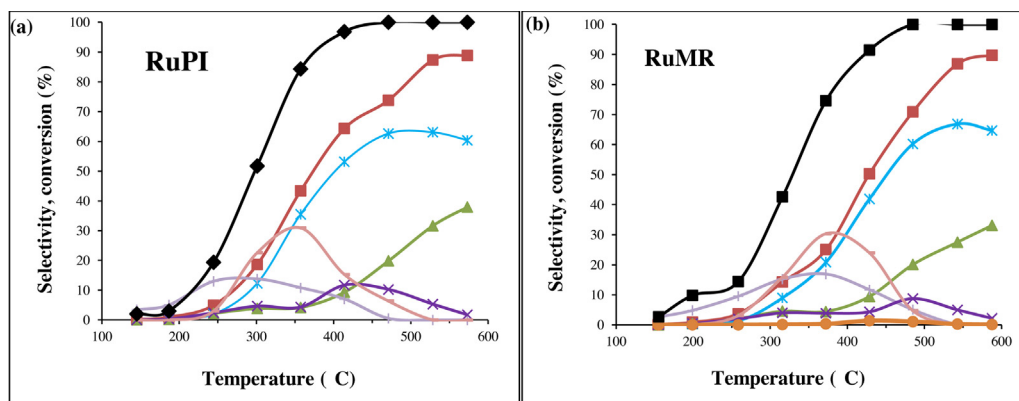


Fig. 2. Catalytic activity in the ethanol steam reforming under soft conditions: ethanol conversion and product selectivity of (a) RuPI and (b) RuMR. Reaction temperature: 150–600 °C, $\frac{W}{F_{\text{EtOH}}^{\text{in}}} = 2447 \text{ g min mol}^{-1}$, molar ratio $\text{H}_2\text{O}/\text{C}_2\text{H}_5\text{OH} = 5$, inlet ethanol concentration = 1%. ♦ Ethanol conversion, selectivities to ■ hydrogen, * carbon dioxide, ▲ carbon monoxide, × methane, + acetaldehyde, — acetone, ● ethylene.

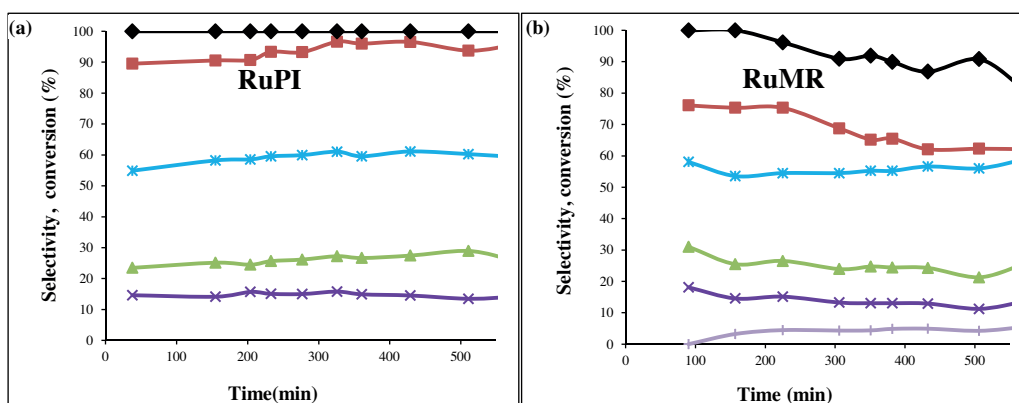


Fig. 3. Catalytic activity and stability in ethanol steam reforming under moderate conditions: ethanol conversion and product selectivity of (a) RuPI and (b) RuMR. Reaction temperature: 600 °C, $\frac{W}{F_{\text{EtOH}}^{\text{in}}} = 49 \text{ g min mol}^{-1}$, molar ratio $\text{H}_2\text{O}/\text{C}_2\text{H}_5\text{OH} = 5$, Inlet ethanol concentration = 7.5%. ♦ Ethanol conversion; selectivities to ■ hydrogen, * carbon dioxide, ▲ carbon monoxide, × methane, + acetaldehyde, — acetone, ● ethylene.

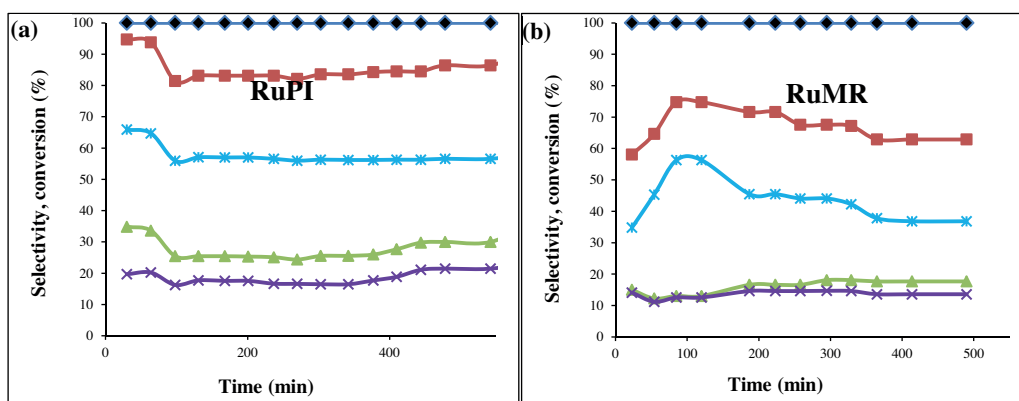


Fig. 4. Catalytic activity and stability in ethanol steam reforming under severe conditions: ethanol conversion and product selectivity of (a) RuPI and (b) RuMR. Reaction temperature: 600 °C, $\frac{W}{F_{\text{EtOH}}^{\text{in}}} = 49 \text{ g min mol}^{-1}$, molar ratio $\text{H}_2\text{O}/\text{C}_2\text{H}_5\text{OH} = 5$, Inlet ethanol concentration = 9.5%. ♦ Ethanol conversion; selectivities to ■ hydrogen, * carbon dioxide, ▲ carbon monoxide, × methane, + acetaldehyde, — acetone, ● ethylene.

time on-stream $S_{\text{H}_2} = 85\%$, CO/CO_2 ratio of 0.48 and $S_{\text{CH}_4} = 18\%$. Acetaldehyde and acetone were not detected and the carbon balance was 100%. RuMR catalyst was tested under equal experimental conditions (Fig. 4b), and ethanol conversion was also completed. Hydrogen selectivity was 65% in average, with a CO/CO_2 ratio of

0.47. As for RuPI, methane formation was observed with a selectivity of 15%.

To compare the temperature effect on the activity and selectivity, RuPI was analyzed at temperatures lower than 600 °C, i.e., 550 °C and 500 °C. Ethanol conversion was complete at 550 °C (see Fig. S4a in Supplementary material), with a hydrogen selectivity

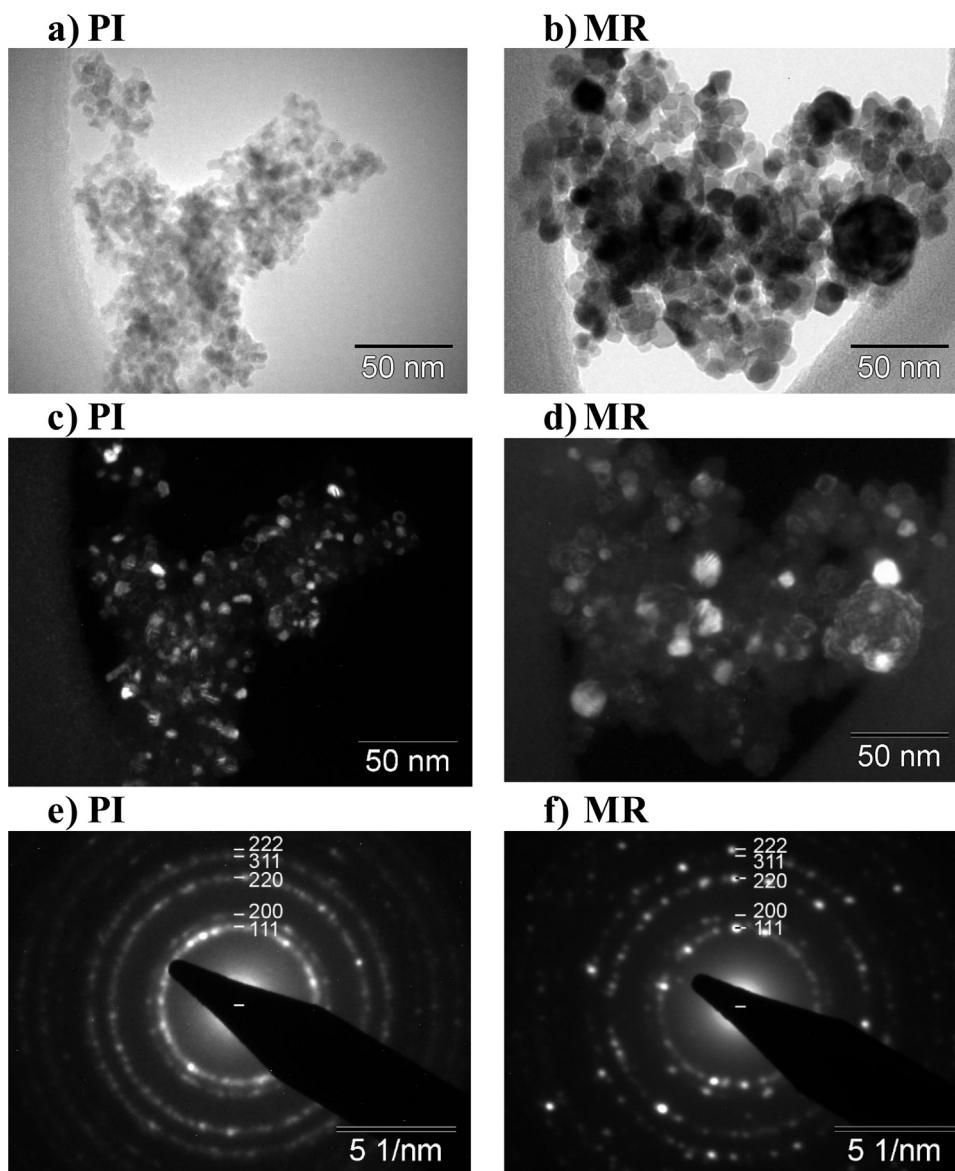


Fig. 5. TEM results corresponding to PI (left) and MR (right). (a) and (b) TEM images. (c) and (d) Corresponding DF images. (e) and (f) SAED patterns indexed with the fluorite type lattice.

of 78% and CO_2 selectivity of 61%. CO and CH_4 were obtained as by-products (acetone and acetaldehyde were not observed). An increase in methane selectivity (25%) and, according to WGS equilibrium (0.3) [71], a significant improvement of the CO/ CO_2 ratio (0.29) were observed. This result could be associated with the CO conversion through WGS, since it is thermodynamically favored ($\Delta H_{\text{reaction}} < 0$) at low temperatures. At 500 °C (see Fig. S4b in Supplementary material), the RuPI performance was poor. The ethanol conversion started in 77% and progressively decreased to 51%. The average hydrogen selectivity was 35%, $S_{\text{CH}_4} = 14\%$ and the CO/ CO_2 ratio 0.15, according to WGS equilibrium (0.15 [71]). Considering these measurements, it could be concluded that in both cases (550 °C and 500 °C reaction temperature) the CO/ CO_2 ratio was improved. However, at 550 °C RuPI maintained its optimum performance, whereas at 500 °C it displayed a poor activity.

Comparing the performance of RuPI and RuMR under soft, moderate and severe conditions for a specific support with $\text{Ce}_{0.8}\text{Zr}_{0.2}\text{O}_2$ composition and independently from the microstructural features (specific area, pore distribution, crystallite size), it is seen that the nature of the active metal is the determining factor of the

ethanol conversion and hydrogen selectivity. However, the differences in the microstructural features of support are reflected in the performance change: for example, the hydrogen selectivity was higher in RuPI rather than in RuMR. This phenomenon could be attributed to the preparation method of the support, which generates a lower specific area and a high crystallite size for MR support. These support characteristics have an undesirable influence in the supported metal microstructure (metallic dispersion and metallic particle size). The PI support has relatively high specific surface area, crystalline size around 5–6 nm and mesoporosity. All these characteristics favor a high metallic dispersion of Ru and improve PI-based catalytic activity. Therefore, under soft operating conditions, the performance of the catalyst is independent of the microstructural and textural support characteristics.

On the one hand, under moderate and severe conditions, a significant improvement in the hydrogen selectivity and an increment in the quantity of by-products (CH_4) were observed for PI supports. Nevertheless, an important improvement in the hydrogen selectivity and in the quantity of secondary products (CH_4) was

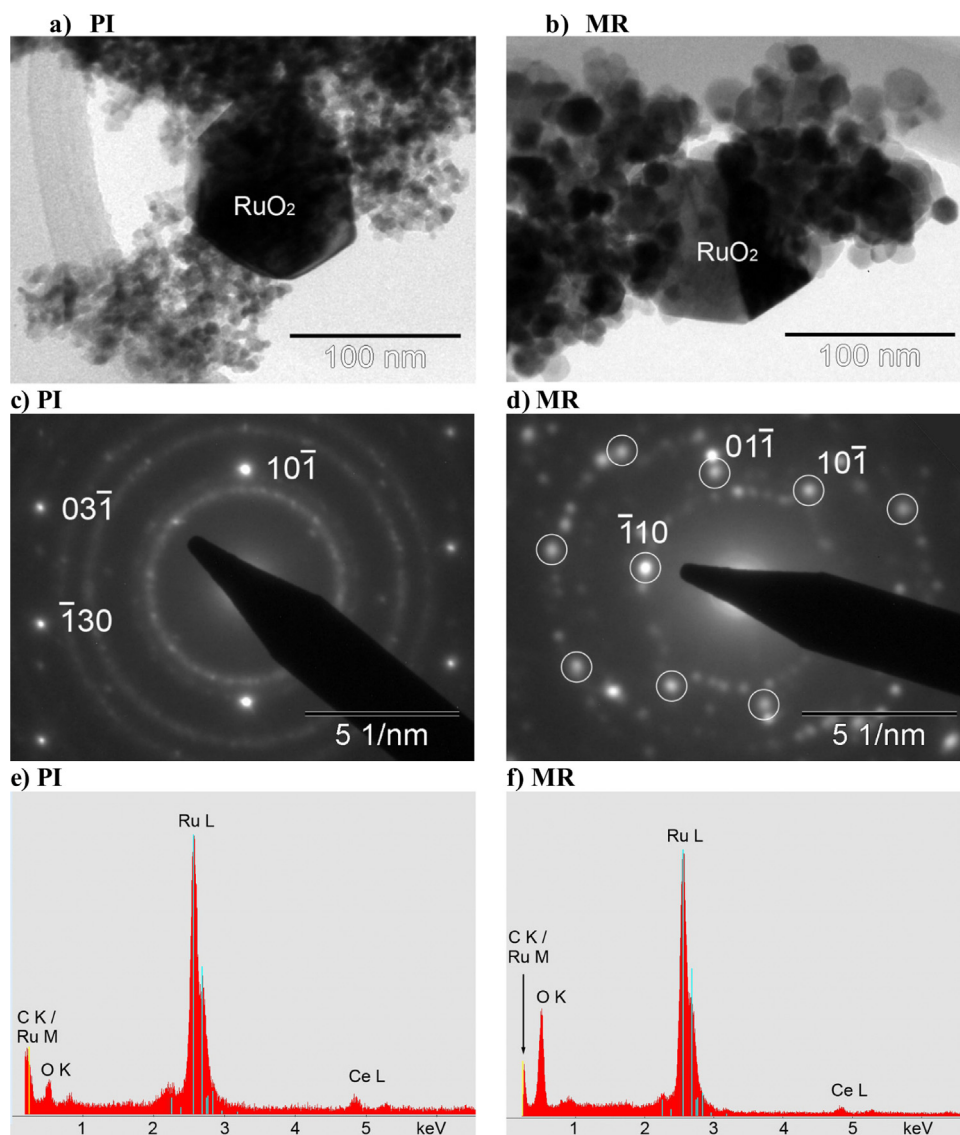


Fig. 6. RuO₂ particle of ~100 nm on the support PI (left) and MR (right). (a) and (b) TEM images. (c) Corresponding SAED pattern showing the [3 1 3] zone axis of the RuO₂ particle and the rings of the PI support. (d) Corresponding SAED pattern showing the [1 1 1] zone axis of the RuO₂ particle and additional reflections of the MR support. (e) and (f) Resulting EDS on the RuO₂ particle.

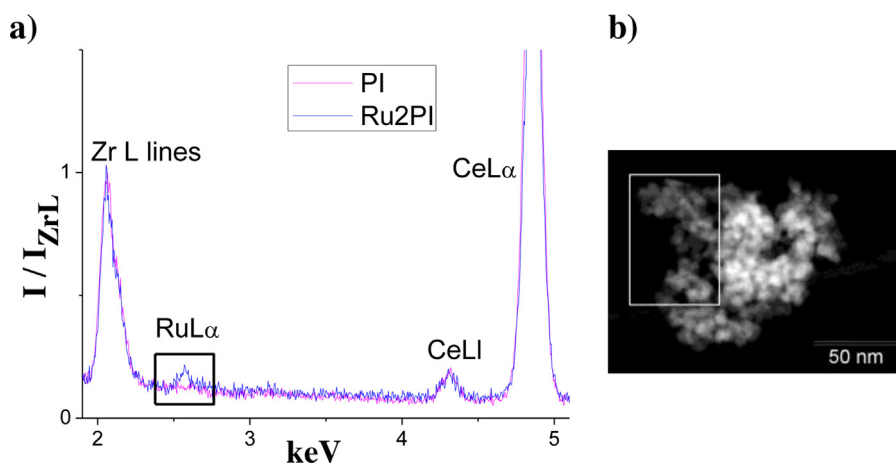


Fig. 7. (a) EDS analysis performed on fresh RuPI (blue line) and PI support (pink line). A weak Ru L line appears in the RuPI spectrum (rectangle). The intensity is normalized to the peak corresponding to the Zr L lines. (b) RuPI high angle annular dark field image. The rectangle indicates the area where the EDS analysis was performed.

observed for PI support when it is operated under moderate and severe conditions.

Taking into account the fact that there are no previous studies of Ru supported over ceria-based materials for ESR, the excellent catalytic performance for ESR observed in Ru samples is a novel result, considering that this metal onto Al_2O_3 showed a moderate performance [6,36].

3.3. Complementary characterization of catalysts and their supports

The microstructure and structural homogeneity of the samples were further investigated employing TEM. Fig. 5a and b show representative TEM images of PI and MR supports, respectively. Fig. 5c and d show their corresponding dark field (DF) images obtained through reflections (1 1 1) and (2 0 0) of the $\text{Ce}_{0.8}\text{Zr}_{0.2}\text{O}_2$ the fluorite type lattice. Both samples showed randomly oriented, rounded nanocrystalline particles. The mean particles size of PI sample was 5 nm (deviation of 2 nm) whereas the mean particles size of MR samples was 13 nm (deviation 7 nm). These results agree with the crystallite size determined by XRPD, suggesting that most of the support nanoparticles are single crystals. The presence of the solid-solution with the fluorite type lattice was confirmed by TEM examinations on different selected area electron diffraction (SAED) patterns (Fig. 5e and f). An accurate match is observed with the fluorite type lattice for all samples. No additional rings were identified after several analyses, which could be associated with the presence of tetragonal or monoclinic phases, reinforcing the idea of structural homogeneity of the samples.

In the RuPI sample, some large RuO_2 particles were easily identified on the support and a RuO_2 particle of 100 nm can be clearly observed (Fig. 6a). The crystal structure of the particle was confirmed by the SAED pattern (Fig. 6c) and the chemical composition by EDS (Fig. 6e). A low intensity O K line could be related to absorption in the particle. Considering that chemisorption measurement shows very small apparent particle size (Table 2) and TPR curve suggests a bimodal distribution in the Ru particles size (Fig. 1), Ru crystallite shown in Fig. 6a should not be representative of all particles containing Ru. Based on previous experimental evidence, two types of RuO_2 are expected to be simultaneously found on RuPI and RuMR (Fig. 6b, d, and e) samples: highly dispersed and large crystalline forms. To detect the presence of small Ru nanoparticles, a small area (50 nm \times 100 nm, approximately) containing only nanoparticles was selected and the EDS analysis was performed. Comparing the result with the EDS obtained on a different specimen, which only contained the support, the Ru L line observed is less intense (Fig. 7). The relative intensity of the signal in the EDS pattern shows that the amount of Ru is small, suggesting that Ru nanoparticles are present on the support in the nanometer range, with sizes lower than or similar to those of the support (Fig. 5a). The highly dispersed ruthenium particles have a higher surface contact with the support, favoring their metal-support interaction.

The surface composition of fresh catalyst was determined measuring the Ru3d, Zr3d, Ce3d and O1s photoelectron peaks. The XPS spectra of RuPI catalyst (Fig. 8) was analyzed in the region of the Ru3d core-level peak, which partially overlaps with the C1s core-level peak. Ru spectrum is composed by two peaks corresponding to the spin-orbit split 3d 5/2 and 3d 3/2 whose positions depend on oxidation state, as indicated with vertical lines in Fig. 8, for component 3d 5/2 and corresponding to Ru^0 , RuO_2 , and RuO_3 . The spectra can be interpreted as a convolution of (using Voigt function for each peak plus a Shirley-type background) the contribution from main peak of carbon (1s) and its satellite, and two pairs of split peaks for Ru. One pair (280.8 eV/284.9 eV) can be assigned to RuO_2 [72], and it is compatible with the presence of the large RuO_2 particles observed in TEM. The other pair (282.2 eV/286.4 eV) correspond to

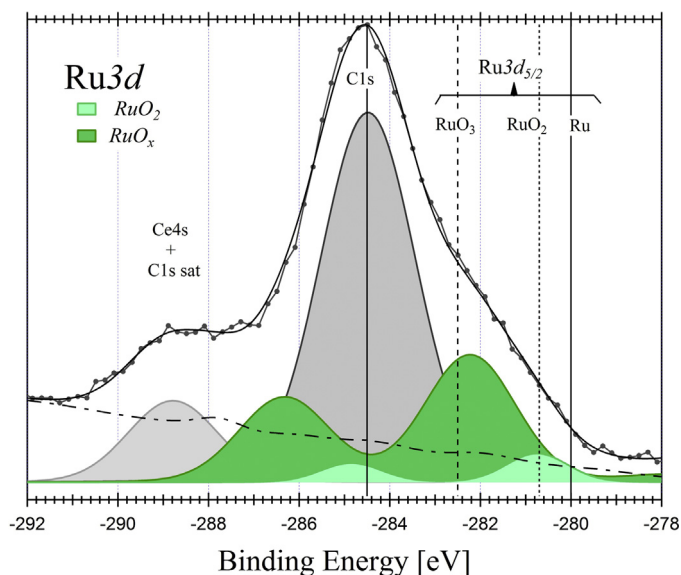


Fig. 8. Ru3d XPS spectra of the RuPI catalyst. X-ray excitation energy was $h\nu = 1253.4$ eV (Mg K α line).

a more oxidized RuO_{2+x} ($0 < x < 1$) [72,73]. The formation of new-chemical-oxide states or intermediate oxides is very common in low dimension systems in which metal-support interactions occur. Alternatively, these last peaks could be interpreted as a shifted RuO_2 contribution ascribed to final state effects due to the small size of the Ru nanoparticles [74]. The C1s peak core can be assigned to both graphitic (from the adhesive carbon tape) and adventitious carbon. The peak at 289 eV, besides of satellite C1s, is also contributed by the Ce4s peak. Another contribution to carbon peaks could be CO_3 species.

3.4. Insights in the RuPI catalyst performance: comparison with NiPI

Numerous publications [10–14,16–27,32] have studied the catalytic behavior for ESR of Ni over different supports, including CeO_2 . In order to compare the performance of our Ru based catalyst with a more studied catalyst, NiPI catalyst was synthesized with the same method and it was tested for ESR under the same experimental conditions. Due to its favorable conditions (absence of impurities, high surface area and improved selectivity to hydrogen), a PI support was selected for the development of this study. High surface area of $\text{Ce}_{0.8}\text{Zr}_{0.2}\text{O}_2$ promotes noble metal dispersion. However, for transition metals, it is not expected in the same extension. To obtain similar metal accessibilities, 8 wt.% of Ni was impregnated. Hence, BET specific surface area was reduced to $85 \text{ m}^2 \text{ g}^{-1}$.

The diffraction pattern of NiPI is displayed in Fig. 9(inset b). It shows the presence of the fluorite type lattice of the $\text{Ce}_{0.8}\text{Zr}_{0.2}\text{O}_2$ support without observable changes and the presence of the principal peaks of NiO. The crystallite sizes of nickel containing particles (17 nm) were calculated by the Scherrer formula. CO chemisorption was employed to evaluate the accessibility of the Ni phases. Metallic dispersion was low, 4.9%. An average metallic size of ≈ 20 nm (in agreement with XRPD) and a specific metallic area of $2.6 \text{ m}^2 \text{ g}^{-1}$ were determined.

TPR profile for NiPI catalyst displays two wide zones centered at 225°C and 357°C (Fig. 9). Since NiO promotes the H_2 spillover on the support, the first reduction zone can be attributed to reduction support and the second reduction zone can be assigned to NiO reduction [75,76]. Maia and Assaf [77] explained the support reduction promoted by NiO via different ways that involve H_2 dis-

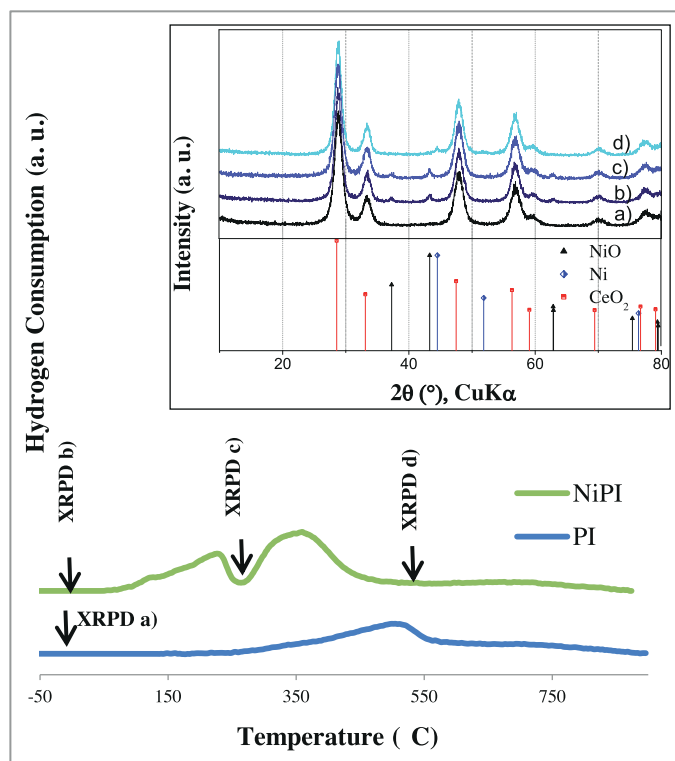


Fig. 9. TPR profiles for PI and NiPI. Inset plot shows XRPD patterns of (a) PI pattern and (b)–(d) NiPI samples indicated in TPR curve, XRPD reference patterns of CeO₂ (PDF 34-0394), Ni (PDF 004-0850), and NiO (PDF 44-1159).

sociation on NiO, H₂ activation at the contact point between NiO and solid-solution or hydrogen spillover from a small number of Ni sites on NiO surface. Three samples were taken during TPR and analyzed by XRPD: before reduction (fresh NiPI), reduced to the end of the first zone (up to 263 °C) and after total reduction (600 °C) (inset Fig. 9, indicated by arrows). The pattern attributed to NiO was observed in the first case (inset Fig. 9, curve a). After the first reduction zone, NiO was also identified (the peak intensity was approximately equal to the first sample), confirming that hydrogen consumption was principally due to surface support reduction (inset Fig. 9, curve b). In this case, the reduction of small particles of NiO (not detectable by XRPD) overlapped with the support reduction cannot be disregarded. Finally, Ni metallic was observed after complete reduction up to 600 °C, in agreement with the assignment of reduction zones.

Fig. 10(a) shows the result of ESR on NiPI under soft conditions. The performances of the catalysts were very similar to Ru based catalyst under the same conditions. NiPI showed a progressive increase in the ethanol conversion up to 480 °C. Simultaneously, H₂ selectivity continuously increased reaching at 543 °C, a maximum of $S_{H_2} = 92.3\%$. Between 200 °C and 500 °C, along with the formation of acetaldehyde, hydrogen, carbon dioxide and acetone, low amounts of by-products were generated, such as methane (selectivities always below 15%). CO production was significant above 300 °C. After complete ethanol conversion (above 480 °C), only H₂, CO and CO₂ were detected in the gas phase, with an expected relative ratio for WGS equilibrium at this temperature.

Fig. 10(b) shows the NiPI catalytic results obtained at 600 °C under severe conditions. Ethanol conversion slightly decreased from an initial value of 100% to 90% after 600 min. Hydrogen selectivity was 70%, CO₂ selectivity was 46% and it was formed along with by-products such as CO and CH₄. CO/CO₂ ratio was 0.37 and methane selectivity was 10%. The amount of acetaldehyde detected was negligible. The carbon balance was 75% which evi-

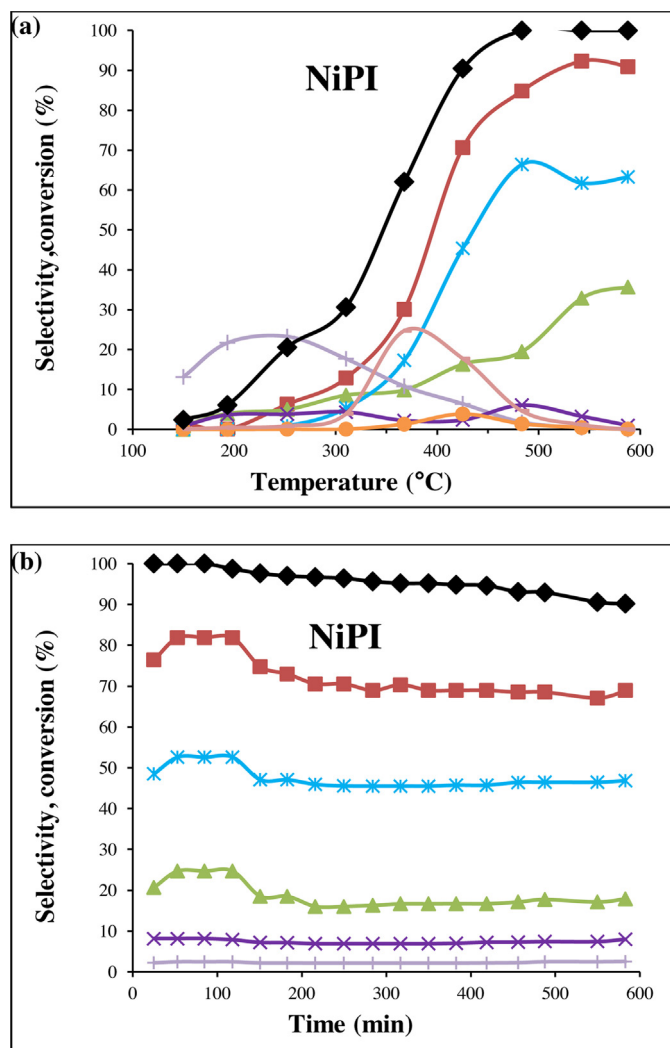


Fig. 10. Catalytic activity and stability in ethanol steam reforming of NiPI under (a) soft conditions (Reaction temperature: 150–600 °C, $\frac{W}{F_{EtOH}} = 2447 \text{ g min mol}^{-1}$, molar ratio H₂O/C₂H₅OH = 5, inlet ethanol concentration = 1%) and (b) severe conditions (Reaction temperature: 600 °C, $\frac{W}{F_{EtOH}} = 49 \text{ g min mol}^{-1}$, molar ratio H₂O/C₂H₅OH = 5, inlet ethanol concentration = 9.5%). ♦ Ethanol conversion; selectivities to: ■ hydrogen, * carbon dioxide, ▲ carbon monoxide, × methane, + acetaldehyde, — acetone, ● ethylene.

dences coke deposit formation. Compared to the values obtained for RuPI catalyst under the same experimental conditions, some relevant differences were observed: the balance carbon for RuPI was 100% and the hydrogen selectivity was 85%.

In order to estimate the amount of carbon deposits, TG measurements under oxygen flow were performed on spent catalysts. Fig. 11 shows RuPI and NiPI thermogravimetric curves. The weight change of the materials was a combination of the weight loss (due to carbon removal) and the weight gain (due to re-oxidation of reduced support and metal nanoparticles). For RuPI, the weight change was very low (0.7%), showing an almost flat profile. For NiPI a net weight change of 36% was determined, of which 38% is attributed to the oxidation of carbonaceous compounds. A combustion average temperature of 550 °C was obtained from the derivative curve of $\Delta \text{weight}/\Delta \text{temperature}$, which indicates a low graphitization degree and allows an easy removal of carbon.

The catalysts used for ESR were analyzed by HR-TEM. After ESR test of NiPI catalyst under severe conditions, the presence of nanocarbon materials was notable (Fig. 12a), with graphitic

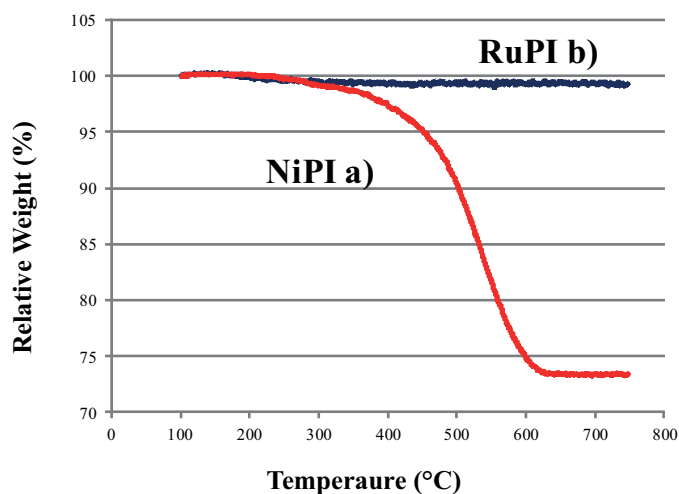


Fig. 11. TGA curves of: (a) NiPI and (b) RuPI, after ESR under severe conditions at 600 °C.

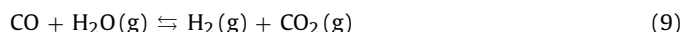
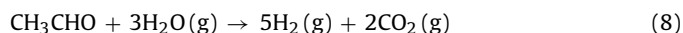
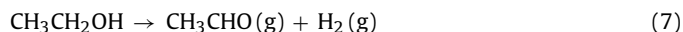
structure of poor structural order. Due to the large coke amount, the carbon production route was impossible to determine [78]. In opposition, RuPI catalyst (after the same ESR test under severe conditions) did not show relevant microstructural changes (Fig. 12b). As expected according to TGA and catalytic testing, carbon deposits were not observed. By comparing RuPI and NiPI it could be concluded that RuPI has an overall better performance. To understand this different behavior, an attempt to analyze the pathway reaction was carried out.

The usual pathway reported for ESR involves the dissociative adsorption of ethanol on the surface generating acetaldehyde, which decomposes to methane and carbon monoxide. Then, CO reacts with water through WGS producing H_2 and CO_2 . Finally, methane is reformed by steam into H_2 , CO and CO_2 , with quantities according to the WGS [35]. An interesting review of the mechanism of ESR for noble and no noble metals over different supports was reported by Mattos et al. [79].

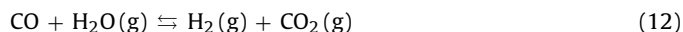
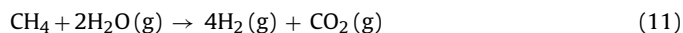
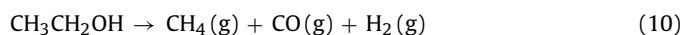
A Ni over ceria ESR catalyst was studied using *in situ* techniques by different authors [27,32]. In particular Xu et al. [27] proposed that ethanol is dissociatively adsorbed by the surface and generates ethoxy species which are dehydrogenated to acetaldehyde and acetyl group (CH_3CO-). After that, acetaldehyde and acetyl are oxidized to acetate. Then, acetate groups are oxidized and C–Cs bond are broken, obtaining carbonate ($-CO_3$) and methyl groups ($-CH_3$). In this context, Ce^{3+} promotes water dissociation and forms OH groups on the surface, which react with methyl group producing CO_2 and inhibiting the methane production. Carbonate groups can

also be decomposed and produce CO_2 . The ceria based supports promote the ethoxy oxidation to acetate below 350 °C [27]. Over 350 °C, metallic nickel catalyzes the acetate C–C dissociation to form carbonates and methyl groups, an improbable process for ceria support. Although there is not any spectroscopic evidence of adsorbed methyl groups, several studies have proposed that adsorbed methyl groups take part of the reaction pathway [79]. The proposed pathway produces mainly CO_2 and H_2 . Xu et al. [27] highlighted the role of ceria, and the strong interaction with Ni. Ceria perturbs the electronic and chemical properties of Ni, decreasing substantially the CO methanation reaction.

Analyzing the ESR results over NiPI (Fig. 10), it can be concluded that the pathway reaction can be suitably described by the one proposed by Xu et al. [27]. The main reactions include the ethanol dehydrogenation into acetaldehyde and its posterior reforming:



The minor methane production observed could be ascribed to ethanol decomposition. Xu et al. [27] proposed that decomposition of ethoxy groups, formed on the surface (dissociative adsorbed ethanol) and not oxidized to acetate, produces methane:



In the case of Ru over ceria based materials, the reaction pathway was not studied by *in situ* techniques. In our previous work, ESR over Ru/CeO₂/YSZ was analyzed and it was proposed that Ru materials did not follow the classic pathway, basically due to the minimum amount of methane in the product distribution. However it is very possible that methane formed is undergoing further steam reforming on Ru [35,49,79]. For this reason, we ran a methane steam reforming test on the catalyst, observing a very poor conversion [80]. In the present work, we observed the same phenomenon for RuPI and RuHW: in soft conditions, the methane quantity was around 10%, whereas the results for NiPI (6%) were slightly inferior. When the conditions were changed, differences in the reaction pathway between Ni and Ru catalyst were observed. For Ni, the highest quantity of methane was about 8%, whereas for RuPI and RuHW the highest quantities were around 15%. Based on these results, a combined mechanism could be suggested. ESR pathway on Ru/Ce_{0.8}Zr_{0.2}O₂ includes ethanol dehydrogenation into acetaldehyde. Therefore, acetaldehyde decomposes into methane, which in turn is reformed into CO and H_2 (classic mechanism).

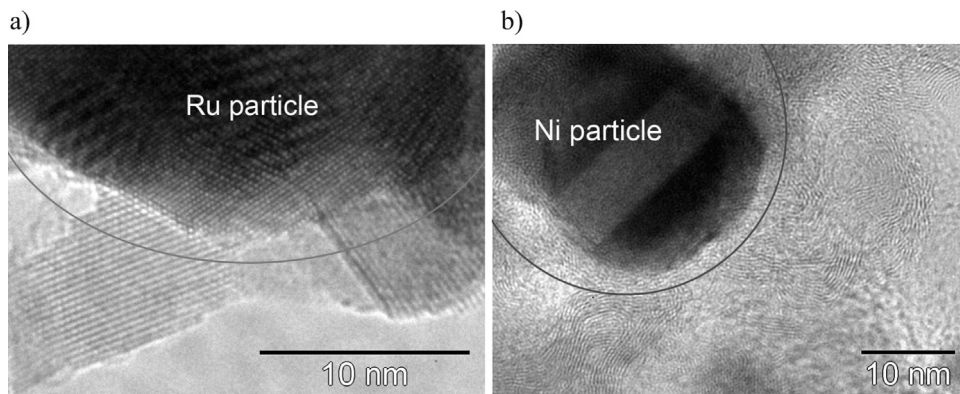


Fig. 12. TEM image of the catalysts after ESR, where the metallic particles are indicated with a circle (a) RuPI (b) NiPI.

Simultaneously, part of the acetaldehyde is reformed by steam to produce H_2 and CO_2 . According to Xu et al. [27], these differences could be associated with the role of the support and the interaction with the metal, since Ce^{3+} promotes this pathway. Both pathway reactions include the WGS. In fact, it has been shown by *in situ* techniques that the reduction of Ce^{4+} at low temperatures induced by the metal-support interaction is critical for the Ru/ CeO_2 catalyst performance in the WGS [42]. Moreover, it is great importance to focus on the absence of carbon deposits, which is a novel result for Ru catalyst in ESR. This behavior could be associated with the nature of the support and its interaction with the metal.

The advance reached here involving a Ru/ $Ce_{0.8}Zr_{0.2}O_2$ nanostructured catalyst with excellent performance in different conditions reactions, became the starting point for *in situ* studies to verify the proposed pathway.

4. Conclusions

The activity of Ru supported over $Ce_{0.8}Zr_{0.2}O_2$ in the ESR was studied. Two $Ce_{0.8}Zr_{0.2}O_2$ supports were produced by different synthesis methods: co-precipitation technique (PI) and mechanochemical reaction (MR). The different supports used have dissimilar microstructural/textural features (specific area, pore distribution, crystallite size), which influence further metal dispersion. In spite of the microstructural differences between the catalysts, the ethanol conversion and the hydrogen selectivity were strongly dependent on both the nature of the active metal and its interaction with the support. On the other hand, the microstructural/textural differences between the supports affected the catalysts performance under severe conditions: for instance, the hydrogen selectivity was higher in RuPI rather than in RuMR. The excellent performance for Ru catalysts in the ESR is a novel result, considering that this metal deposited in Al_2O_3 has demonstrated a moderate performance.

The activity and stability of Ru based catalyst were also compared with Ni based catalyst. The comparison of RuPI and NiPI shows that RuPI has an overall better performance. Analyzing the results, it is concluded that both catalysts follow a different pathway reaction. Ni based catalyst follows the pathway proposed by Xu et al., (ethanol dehydrogenates into acetaldehyde and it is reformed, observing buildup of carbonaceous residues) whereas for Ru catalyst, the reaction pathway includes ethanol dehydrogenation into acetaldehyde. In the next step, the decomposition of acetaldehyde into methane as well as acetaldehyde reforming by steam are involved. No deposition of carbon was detected for RuPI catalyst.

The excellent results obtained for Ru/ $Ce_{0.8}Zr_{0.2}O_2$ in ESR as a consequence of a favorable combination of the high metallic dispersion and the high support properties; allow the employment of lower-cost noble catalyst, without increasing the metallic charge.

Acknowledgements

The authors acknowledge CONICET (National Council of Scientific and Technological Research), CNEA (National Commission of Atomic Energy), ANPCyT (National Agency of Science and Technology Promotion), Instituto Balseiro (University of Cuyo), University of San Luis, University of Trieste and Ministry of Foreign Affairs of Italy. I.A.C-R and F.C.G thank Prof. P. Fornasiero and Dr. T. Montini for the hospitality during the visit of I.A.C-R to Prof. Fornasiero's research group at Department of Chemical and Pharmaceutical Sciences and ICCOM Trieste Research Unit (University of Trieste), where in particular the catalytic data contained in Fig. 2 and Fig. 10a were collected. The authors thank also Facundo Castro for his assistance in TG measurements. Helpful discussion on English redaction

with María del Carmen Ferreiro, Nancy González and María Laura Tovar-Toulouse is acknowledged.

Appendix A. Supplementary data

Supplementary data associated with this article can be found, in the online version, at <http://dx.doi.org/10.1016/j.apcatb.2015.07.025>.

References

- [1] C. Song, Hydrogen and Syngas Production and Purification Technologies, in: K. Liu, C. Song, V. Subramani (Eds.), 1st ed., John Wiley & Sons Inc., New Jersey, 2010, pp. 1–13.
- [2] S. Cavallaro, V. Chiodo, S. Freni, N. Mondello, F. Frusteri, Appl. Catal. A: Gen. 249 (2003) 119–128.
- [3] C. Diagne, H. Idriss, A. Kiennemann, Catal. Commun. 3 (2002) 565–571.
- [4] J.C. Vargas, S. Libs, A.C. Roger, A. Kiennemann, Catal. Today 417 (2005) 107–108.
- [5] M. Benito, J.L. Sanz, R. Isabel, R. Padilla, R. Arjona, L. Daza, J. Power Sources 151 (2005) 11–17.
- [6] P. Vaidya, A. Rodrigues, Ind. Eng. Chem. 45 (2006) 6614–6618.
- [7] S. Cavallaro, Energy Fuels 14 (2000) 1195–1199.
- [8] H. Idriss, Platinum Met. Rev. 48 (2004) 105–115.
- [9] D. Liguras, D. Kondarides, E. Verykios, Appl. Catal. B Environ. 43 (2003) 345–354.
- [10] A. Aboudheir, A. Akande, R. Idem, A. Dalai, Int. J. Hydrogen Energy 31 (2006) 752–761.
- [11] J. Comas, M.L. Dieuzeide, G. Baronetti, M. Laborde, N. Amadeo, Chem. Eng. J. 118 (2006) 11–15.
- [12] Y. Yang, J. Ma, F. Wu, Int. J. Hydrogen Energy 31 (2006) 877–882.
- [13] M.N. Barroso, M.F. Gomez, L.A. Arrúa, M.C. Abello, Appl. Catal. A: Gen. 304 (2006) 116–123.
- [14] D.A. Morgenstern, J.P. Fornango, Energy Fuels 19 (2005) 1708–1716.
- [15] M.S. Batista, R.K.S. Santos, E.M. Assaf, J.M. Assaf, E.A. Ticianelli, J. Power Sources 134 (2004) 27–32.
- [16] J. Kugai, S. Velu, C. Song, Catal. Lett. 101 (2005) 255–264.
- [17] F. Mariño, G. Baronetti, M. Jobbagy, M. Laborde, Appl. Catal. A: Gen. 238 (2003) 41–54.
- [18] F. Frusteri, S. Freni, L. Spadaro, V. Chiodo, G. Bonura, S. Donato, S. Cavallaro, Catal. Commun. 5 (2004) 611–615.
- [19] V. Palma, F. Castaldo, P. Ciambellia, G. Iaquaniello, Appl. Catal. B: Environ. 145 (2014) 73–84.
- [20] B. Zhang, X. Tang, Y. Li, W. Cai, Y. Xu, W. Shen, Catal. Commun. 7 (2006) 367–372.
- [21] F. Frusteri, S. Freni, V. Chiodo, S. Donato, G. Bonura, S. Cavallaro, Int. J. Hydrogen Energy 31 (2006) 2193–2199.
- [22] L.P.R. Profeti, E.A. Ticianelli, E.M. Assaf, Int. J. Hydrogen Energy 34 (2009) 5049–5060.
- [23] H.V. Fajardo, L.F.D. Probst, N. Carreño, I.T.S. Garcia, A. Valentini, Catal. Lett. 119 (2007) 228–236.
- [24] P. Biswas, D. Kunzru, Int. J. Hydrogen Energy 32 (2007) 969–980.
- [25] G. Garbarino, S. Campodonico, A.R. Perez, M.M. Carnasciali, P. Riani, E. Finocchio, G. Busca, Appl. Catal. A: Gen. 452 (2013) 163–173.
- [26] A. Galetti, M. Gómez, L. Arrúa, M.C. Abello, Appl. Catal. A Gen. 380 (2010) 40–47.
- [27] W. Xu, Z. Liu, A.C. Johnston-Peck, S.D. Senanayake, G. Zhou, D. Stacchiola, E.A. Stach, J.A. Rodriguez, ACS Catal. 3 (2013) 975–984.
- [28] Y. Ando, K. Matsuoka, H. Takaig, K. Kuramoto, Bull. Chem. Soc. Jpn. 85 (2012) 517–521.
- [29] F. Auprêtre, C. Descorme, D. Duprez, Catal. Commun. 3 (2002) 263–267.
- [30] S. De Lima, A.M. da Silva, U.M. Graham, G. Jacobs, B.H. Davis, L.V. Mattos, F.B. Noronha, Appl. Catal. A: Gen. 352 (2009) 95–113.
- [31] H. Idriss, M. Scott, J. Llorca, S. Chan, W. Chiu, P. Sheng, A. Yee, M. Blackford, S. Pas, A. Hill, F. Alamgir, R. Rettew, C. Petersburg, S. Senanayake, M.A. Barbeau, ChemSusChem 1 (2008) 905–910.
- [32] G. Busca, T. Montanari, C. Resini, G. Ramis, U. Constantino, Catal. Today 143 (2009) 2–8.
- [33] A.C.W. Koh, L. Chen, W.K. Leong, T.P. Ang, B.F.G. Johnson, T. Khimyak, J. Lin, Int. J. Hydrogen Energy 34 (2009) 5691–5703.
- [34] A.C. Basagiannis, P. Panagiotopoulou, X.E. Verykios, Top Catal. 51 (2008) 2–12.
- [35] T. Montini, L. De Rogatis, V. Gombac, P. Fornasiero, M. Graziani, Appl. Catal. B: Environ. 71 (2006) 125–134.
- [36] M. Bilal, S. Jackson, Catal. Sci. Tech. 2 (2012) 2043–2051.
- [37] J. Kaspar, in: K.A. Gschneider Jr, L. Eyring (Eds.), Handbook of the Physics and Chemistry of Rare Earths, vol. 29, Elsevier Science B.V., 2002, pp. 159–266.
- [38] A. Trovarelli, Catalysis by Ceria and Related Materials, 2nd ed, Imperial College Press, London, 2002.
- [39] G. Colon, M. Pijolat, F. Valdivieso, H. Vidal, J. Kaspar, E. Finocchio, M. Daturi, C. Binet, J.C. LaValley, R.T. Baker, S. Bernal, J. Chem. Soc. Faraday Trans. 94 (1998) 3717–3726.
- [40] J. Kaspar, P. Fornasiero, M. Graziani, Catal. Today 50 (1999) 285–298.

- [41] S. Oh, G. Hoflund, *J. Phys. Chem.* 110 (2006) 7609–7613.
- [42] W. Xu, R. Si, S.D. Senanayake, J. Llorca, H. Idriss, D. Stacchiola, J.C.A. Hanson, J.A. Rodriguez, *J. Catal.* 291 (2012) 117–126.
- [43] Y. Chen, H. Wang, R. Burch, C. Hardacre, P. Hu, *Faraday Discuss.* 152 (2011) 121–133.
- [44] J. Vecchiotti, A. Bonivardi, W. Xu, D. Stacchiola, J.J. Delgado, M. Calatayud, S.E. Collins, *ACS Catal.* 4 (2014) 2088–2096.
- [45] J.A. Rodriguez, *Catal. Today* 160 (2011) 3–10.
- [46] N. Laosiripojana, S. Assabumrungrat, *Appl. Catal. B Environ.* 66 (2006) 29–39.
- [47] J. Kim, D. Lee, *Int. J. Hydrogen Energy* 38 (2013) 11853–11862.
- [48] M. Mogensen, *Catalysis by Ceria and Related Materials*, in: A. Trovarelli (Ed.), 2nd ed., Imperial College Press, London, 2002.
- [49] I.A.C. Ramos, T. Montini, B. Lorenzuti, H. Troiani, F.C. Gennari, M. Graziani, P. Fornasiero, *Catal. Today* 180 (2012) 96–104.
- [50] P. Yaseneva, S. Pavlova, V. Sadykov, G. Alikina, A. Lykashevich, V. Rogov, S. Belochapkine, J. Ross, *Catal. Today* 137 (2008) 23–28.
- [51] F.C. Gennari, A. Carbajal Ramos, A. Condó, T. Montini, S. Bengió, A. Cortesi, J.J. Andrade Gamboa, P. Fornasiero, *Appl. Catal. A: Gen.* 398 (2011) 123–133.
- [52] I.A. Carbajal-Ramos, J.J. Andrade Gamboa, F.C. Gennari, *Mater. Chem. Phys.* 137 (2013) 1073–1080.
- [53] J. Laugier, B. Bochu, LMGP-Suite Suite of Programs for the interpretation of X-ray Experiments, ENSP/Laboratoire des Matériaux et du Génie Physique, BP 46, 38,042 Saint Martin d'Hères, France <<http://www.ccp14.ac.uk/tutorial/lmgp/>>.
- [54] J.I. Langford, R.D.E. Delhez, T.H. Keijser, E.J. Mittemeijer, *Aust. J. Phys.* 41 (1988) 173–187.
- [55] J.M. Gatica, R.T. Baker, P. Fornasiero, S. Bernal, J. Kaspar, *J. Phys. Chem. B* 105 (649) (2001) 1191–1199.
- [56] M. Yashima, N. Ishizawa, M. Yoshimura, *J. Am. Ceram. Soc.* 75 (1992) 1550–1557.
- [57] J. Rouquerol, D. Avnir, C.W. Fairbridge, D.H. Everett, J.H. Haynes, N. Pernicone, J.D.F. Ramsay, K.S.W. Sing, K.K. Unger, *Pure Appl. Chem.* 66 (1994) 1739–1758.
- [58] K.S.W. Sing, D.H. Everett, R.A.W. Haul, L. Moscou, R.A. Pierotti, J. Rouquerol, T. Siemieniowska, *Pure Appl. Chem.* 57 (1985) 603–619.
- [59] G. Leofanti, M. Padovan, G. Tozzola, B. Venturelli, *Catal. Today* 41 (1998) 207–219.
- [60] P. Fornasiero, T. Montini, M. Grazianu, J. Kaspar, A.B. Hungria, A. Martínez-Arias, J.C. Conesa, *Phys. Chem. Chem. Phys.* 4 (2002) 149–159.
- [61] P. Singh, M.S. Hegde, *J. Solid State Chem.* 181 (2008) 3248–3256.
- [62] X. Q. Wang, W. Li, W. Li, J. Feng, *Catal. Commun.* 50 (2014) 21–24.
- [63] S. Aouad, E. Abi-Aad, A. Aboukais, *Appl. Catal. B: Environ.* 88 (2009) 249–256.
- [64] M. Kurnatowska, W. Mista, P. Mazur, L. Kepinski, *Appl. Catal. B: Environ.* 148–149 (2014) 123–135.
- [65] G. Jacobs, A. Sarkar, Y. Ji, M. Luo, A. Dozier, B.H. Davis, *Ind. Eng. Chem. Res.* 47 (2008) 672–680.
- [66] A. Trovarelli, G. Dolcetti, C. de Leitenburg, J. Kaspar, *Stud. Surf. Sci. Catal.* 75 (1993) 2781–2784.
- [67] S. Hosokawa, Y. Fujinami, H. Kanai, *J. Mol. Catal. A Chem.* 240 (2005) 49–54.
- [68] H. Idriss, C. Diagne, J.P. Hindermann, A. Kiennemann, M.A. Barteau, *J. Catal.* 155 (1995) 219–237.
- [69] R. Pestman, R.M. Koster, E. Boellaard, A.M. van der Kraan, V. Poncet, *J. Catal.* 174 (1998) 142–152.
- [70] E.J. Grootendorst, R. Pestman, R.M. Koster, V. Poncet, *J. Catal.* 148 (1994) 261–269.
- [71] C. Rossi, C. Alonso, O. Antunes, R. Guirardello, L. Cardozo-Filho, *Int. J. Hydrogen Energy* 34 (2009) 323–332.
- [72] S.-F. Weng, Y.-H. Wang, C.-S. Lee, *Appl. Catal. B Environ.* 134 (2013) 359–366.
- [73] K. Qadir, S.H. Joo, B.S. Mun, D.R. Butcher, J.R. Renzas, F. Aksoy, Z. Liu, G.A. Somorjai, J.Y. Park, *Nano Lett.* 12 (2012) 5761–5768.
- [74] G.K. Wertheim, S.B. DiCenzo, S.E. Youngquist, *Phys. Rev. Lett.* 51 (1983) 2310–2313.
- [75] T. Takeguchi, S. Furukawa, M. Inoue, *J. Catal.* 202 (2001) 14–24.
- [76] A. Tarditi, M.N. Barroso, A.E. Galetti, L. Arrúa, L. Cornaglia, M.C. Abello, *Surf. Interface Anal.* 46 (8) (2014) 521–529.
- [77] T.A. Maia, E.M. Assaf, *RSC Adv.* 4 (2014) 31142.
- [78] M.D. Sánchez, M.S. Moreno, I. Costilla, C.E. Gigola, *Catal. Today* 133–135 (2008) 842–845.
- [79] L.V. Mattos, G. Jacobs, B.H. Davis, F.B. Noronha, *Chem. Rev.* 112 (2012) 4094–4123.
- [80] I.A. Carbajal-Ramos, PhD Thesis, Instituto Balseiro, Universidad Nacional de Cuyo, Argentina (2014) <<http://ricabib.cab.cnea.gov.ar/484/>>.